

Weyl nodes in $\text{Ce}_3\text{Bi}_4\text{Pd}_3$ revealed by dynamical mean-field theoryMartin Braß¹, Jan M. Tomczak^{2,1} and Karsten Held¹¹*Institute of Solid State Physics, TU Wien, 1040 Vienna, Austria*²*Department of Physics, King's College London, Strand, London WC2R 2LS, United Kingdom*

(Received 16 April 2024; accepted 7 August 2024; published 29 August 2024)

Experimental studies have found unusual transport properties in $\text{Ce}_3\text{Bi}_4\text{Pd}_3$ which are potentially a consequence of the interplay between band-structure topology and electronic correlations. Based on these measurements, the existence of Weyl points in strongly renormalized, flat quasiparticle bands has been postulated. However, so far there has been neither a direct spectroscopic observation of these nor a calculation from first principles that would confirm their existence close to the Fermi energy. Here we present density functional theory and dynamical mean-field theory calculations and study the low-energy excitations and their topological properties. We find that the Kondo effect promotes two out of the six angular momentum $J = 5/2$ states, with the other four pushed to higher energies. Further, we find Weyl nodes close to the Fermi energy as previously suggested for explaining the observed giant spontaneous Hall effect in $\text{Ce}_3\text{Bi}_4\text{Pd}_3$ as well as nodal lines.

DOI: [10.1103/PhysRevResearch.6.033227](https://doi.org/10.1103/PhysRevResearch.6.033227)

I. INTRODUCTION

Weyl-Kondo semimetals interface topology and strong correlation physics and exhibit low-energy excitations and transport properties different from weakly interacting materials [1–6]. The Coulomb interaction between localized f electrons and their hybridization with conduction bands results in flat bands and quasiparticles with very high effective masses and, accordingly, low renormalized velocities. These bands can cross each other at isolated points close to the Fermi energy giving rise to a linear dispersion relation of the quasiparticles which then behave like Weyl fermions [7,8]. Such Weyl points are monopoles of Berry curvature [9], potentially providing significant contributions to the transverse electrical conductivity in Hall experiments, even without an external magnetic field [10].

One Weyl-Kondo semimetal candidate is the noncentrosymmetric compound $\text{Ce}_3\text{Bi}_4\text{Pd}_3$ [1] whose crystal structure [11] is shown in Fig. 1. The absence of inversion symmetry makes the existence of Weyl points possible and the nominally single, localized Ce- $4f$ valence electron gives rise to the Kondo effect at low temperatures [1]. When the system is cooled to the Kondo coherent regime, measurements of the specific heat show a cubic dependence on temperature. While usually this is a consequence of phonons, in the case of $\text{Ce}_3\text{Bi}_4\text{Pd}_3$, the comparison to the reference material $\text{La}_3\text{Bi}_4\text{Pt}_3$ indicates that the electronic contribution to the specific heat dominates the phononic one [1]. Hence, these observations have been attributed to the existence of Weyl

fermions with quasiparticle velocities reduced by three orders of magnitude compared to weakly interacting metals [1].

Further evidence for this interpretation came from electrical conductivity measurements that showed a giant, spontaneous Hall effect [5]. Tilted Weyl points close to the Fermi edge could induce significant amounts of Berry curvature on the Fermi surface, which could explain the observed transverse electric current in the absence of magnetic fields [5,6].

However, so far there has been neither a direct spectroscopic observation of these Weyl nodes in highly renormalized bands, nor a calculation from first principles that would confirm their existence in the vicinity of the Fermi energy. Here we study $\text{Ce}_3\text{Bi}_4\text{Pd}_3$ by the combination [12,13] of density functional theory (DFT) and dynamical mean-field theory (DMFT) that captures both the topological properties of the material, as well as the electronic correlations and Kondo physics. For the localized $4f$ electrons of Ce, the local DMFT correlations can be expected to provide an accurate description, as long as we are not in the vicinity of an ordering instability with strong nonlocal correlations.

Our results are strikingly different from a previous DFT+DMFT study [14] that did not discriminate between the self-energies of the different $J = 5/2$ states (J : total angular momentum). As we will see below such a differentiation is essential to describe the Kondo effect in $\text{Ce}_3\text{Bi}_4\text{Pd}_3$ correctly. Further, in Ref. [14] topology has been studied only in the (effective one-particle) DFT not in the (interacting) DFT+DMFT electronic structure.

The outline of the paper is as follows: In Sec. II we describe the DFT electronic structure and discuss the symmetry properties of the local orbitals that will give rise to a Kondo resonance. In Sec. III we study the interacting band structure within DMFT. We derive an effective low-energy Hamiltonian in Sec. IV, which allows us to analyze its topology. We discover Weyl points from the renormalized quasiparticle

Published by the American Physical Society under the terms of the Creative Commons Attribution 4.0 International license. Further distribution of this work must maintain attribution to the author(s) and the published article's title, journal citation, and DOI.

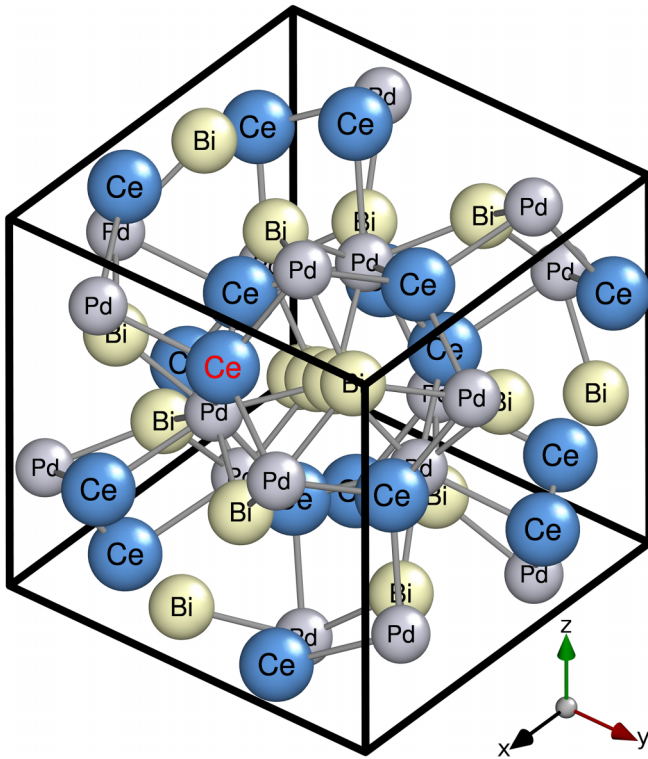


FIG. 1. Crystal structure [11] in the conventional unit cell of $\text{Ce}_3\text{Bi}_4\text{Pd}_3$. One of the equivalent Ce atom is highlighted for reference in Sec. II.

bands in Sec. V and nodal lines in Sec. VI. A summary and discussion of our results can be found in Sec. VII.

II. TIGHT-BINDING MODEL FROM FIRST PRINCIPLES

To study how electronic correlations of the localized Ce-4*f* orbitals influence the topological properties, we need an accurate and material-realistic model that captures the hybridization between these. As a starting point, we perform a self-consistent density functional theory (DFT) calculation using the full potential local orbital (FPLO) code [15]. The system has space group $I\bar{4}3d$ (220), and we use $a = 10.051$ Å as lattice parameter. The Wyckoff positions of the different atoms are Ce: (3/8, 0, 1/4), Bi: (1/12, 1/12, 1/12), Pd: (7/8, 0, 1/4).

We employ a dense ($6 \times 6 \times 6$) k -mesh and the Perdew-Wang exchange-correlation potential [16] within the local density approximation (LDA) to determine the electronic band structure. After the calculation is converged, we take the resulting ground state density as the starting point for another self-consistent computation, where we increase the k mesh to ($12 \times 12 \times 12$). This computation converges immediately, thereby confirming that the initial k mesh is sufficient. All calculations are fully relativistic, which especially includes spin-orbit coupling (SOC).

In Fig. 2 we show the corresponding band structure. We obtain an insulating system in DFT, because hybridization between Ce-4*f* orbitals and conduction bands compresses the latter and opens a gap. By looking at the density of states (DOS) in the right panel of Fig. 2, we can see that the Ce-4*f*

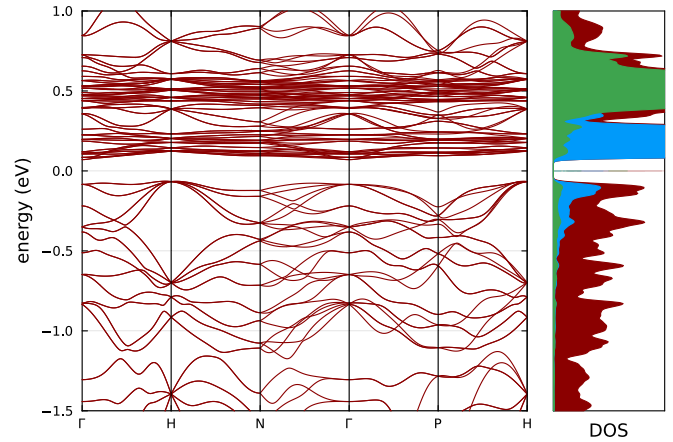


FIG. 2. Electronic band structure calculated within DFT. In the primitive basis the coordinates of the high-symmetry points are $H = (1/2, -1/2, 1/2)$, $P = (1/4, 1/4, 1/4)$, $\Gamma = (0, 0, 0)$, $N = (0, 0, 1/2)$. The Ce-4*f* orbitals hybridize with the conduction bands, which leads to a band gap. The right panel shows the total density of states (red) as well as the partial densities for the Ce-4*f*_{5/2} (blue) and Ce-4*f*_{7/2} (green) orbitals.

orbitals in $\text{Ce}_3\text{Bi}_4\text{Pd}_3$ have a contribution close to the Fermi energy. If electronic correlations are later included, these will give rise to a narrow Kondo peak at the Fermi energy. However, in order to describe this Kondo physics, we need to treat the electronic correlations more accurately than it is possible within DFT.

To capture the low-energy degrees of freedom of the system, we perform a Wannierization of the bands (cf. Appendix A for the quality of the Wannier projection). As there are many entangled bands around the Fermi energy, we here project them onto the 4*f* orbitals of the six Ce atoms, the 4*d* orbitals of the six Pd atoms and the 6*p* orbitals of the eight Bi atoms in the unit cell. This yields altogether 192 Wannier orbitals out of which 6×14 correspond to the Ce-4*f*. For the latter, correlations need to be treated beyond a static mean-field approximation. This large number of correlated orbitals makes computations very demanding. However, we can simplify the problem by observing that SOC nicely separates 4*f*_{5/2} and 4*f*_{7/2} orbitals in energy as can be seen in the DOS from Fig. 2. The 4*f*_{7/2} orbitals are farther above the Fermi energy, such that only the 4*f*_{5/2} orbitals will be occupied at low temperatures. This energy separation allows us to treat only the correlations of the 4*f*_{5/2} orbitals on the level of dynamical mean-field theory (DMFT) and the Coulomb repulsion between 4*f*_{7/2} and 4*f*_{5/2} orbitals on a static mean-field level.

By analyzing the symmetry properties of the 4*f*_{5/2} orbitals, we can identify which of them can interact with each other and which cannot. For this, we compute the stabilizer group of the Ce atoms, i.e., the subgroup of space group $I\bar{4}3d$ (220), which leaves the position of a Ce atom invariant. In the present case the stabilizer is generated by a single fourfold screw roto-inversion axis, that is, a fourfold rotation, followed by inversion and translation by a fractional lattice vector. In other words, the stabilizer is isomorphic to S_4 .

Hence, the Ce-4*f* orbitals form a representation of this group. However, as SOC is not negligible, the group of relevance here is the double cover of S_4 for which the $4f_{5/2}$ orbitals form a representation which we can decompose into irreducible representations (irreps) using the calculus of characters. Since S_4 is abelian, all irreps are one-dimensional. Additionally, due to time-reversal symmetry, for every irrep contained in the space spanned by the $4f_{5/2}$ orbitals its dual representation must be contained as well such that these are degenerate in the local crystal field. Thus the latter will split the $4f_{5/2}$ manifold into three twofold degenerate states. A direct calculation reveals that the decomposition reads

$$\Gamma_7 \oplus \Gamma_7^* \oplus \Gamma_6^{\oplus 2} \oplus (\Gamma_6^*)^{\oplus 2}. \quad (1)$$

Here we used the notation for irreps from Cracknell [17], a star denotes the dual representation, \oplus is the direct sum of vector spaces, and the exponent $\oplus 2$ indicates that an irrep occurs twice in the decomposition.

To get a better intuition of what these irreps are, we exemplarily pick the Ce atom highlighted in Fig. 1 in red. For this atom, the S_4 axis is parallel to the x axis. Then we can choose the spin-quantization axis to be the x axis as well and observe that the $j_x = 1/2$ spans the Γ_7 irrep and $j_x = -1/2$ spans its dual. Furthermore, both $j_x = 3/2$ and $j_x = -5/2$ transform as Γ_6 . Therefore, these orbitals can interact and will hybridize due to the local crystal field thereby forming linear combinations:

$$\begin{aligned} \psi_+ &= \alpha |j_x = 3/2\rangle + \beta |j_x = -5/2\rangle, \\ \psi_- &= \beta |j_x = 3/2\rangle - \alpha |j_x = -5/2\rangle. \end{aligned} \quad (2)$$

These are the eigenorbitals of the local Hamiltonian projected onto the Ce-4*f* manifold. The coefficients α , β , and onsite energies can be obtained from our Wannier-Hamiltonian. ψ_- is lower in energy than the $j_x = 1/2$ orbital, which in turn is lower in energy than the ψ_+ orbital. The same linear combinations can also be constructed for opposite j_x , which then transform as the dual irrep Γ_6^* .

To speed up the following DMFT calculation we take advantage of the above observations. If we transform the Wannier orbitals into the basis of ψ_- , ψ_+ and $j_x = \pm 1/2$ orbital, then locally the Ce-4*f* part of the Hamiltonian is diagonal. During the DMFT cycle the $j_x = 1/2$ orbital will not obtain off-diagonal terms, since it belongs to an irrep which occurs only once in the decomposition of the $4f_{5/2}$ manifold. For the ψ_- and the ψ_+ orbital off-diagonal elements might be generated, since these orbitals can hybridize further. For quantifying the importance of these off-diagonal terms, we computed the average of the absolute values of diagonal and off-diagonal terms of the local Green's function over all Matsubara frequencies with energies between -10 eV and $+10$ eV. The mean of the diagonal terms is by a factor of 263 higher than the off-diagonal one. Hence, we will neglect the off-diagonal terms in the DMFT calculation. This reasonable approximation gives a considerable performance boost, which allows us to go to low temperatures.

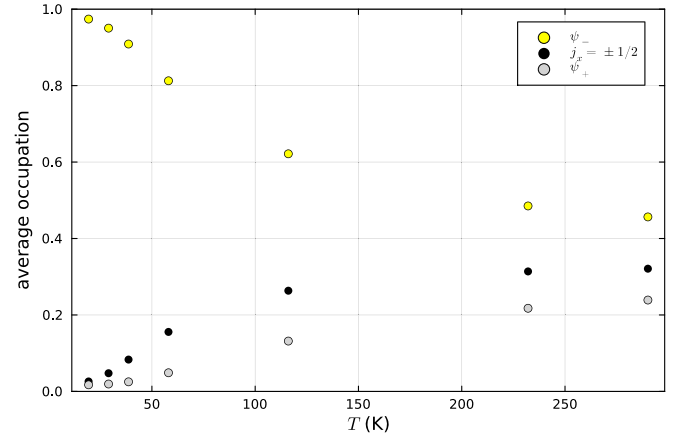


FIG. 3. Average occupation of the Ce- $4f_{5/2}$ orbitals as a function of temperature within DMFT.

III. CALCULATIONS WITH DMFT

With the Wannier Hamiltonian from the previous section we have a model at hand which is derived from first principles and can be used as starting point for a DMFT calculation. Here we use the quantum Monte Carlo (QMC) continuous time hybridization expansion (CT-Hyb) as impurity solver using the w2DYNAMICS implementation [18]. The electronic interaction is modeled by a density-density interaction with Coulomb repulsion parameter $U = 6$ eV, similar to values used previously for various Ce₃A₄M₃ compounds [14,19–21]. Double counting is taken into account as described by Anisimov *et al.* [22]. Since Ce is in a dominantly $4f^1$ configuration, we neglect Hund's exchange for the sake of reaching lower temperatures in DMFT. That is, the interaction term is $H_U = U \sum_{i\alpha < \beta} n_{i\alpha} n_{i\beta}$ where $n_{i\alpha}$ is the occupation number operator for an electron at Ce site i in the spin orbital α (out of 14, of which six $J = 5/2$ are treated on the DMFT and eight $J = 7/2$ on the static mean-field level). This simplified interaction is justified as long as we are not looking into the multiplet splitting of the upper Hubbard bands. Using Pulay mixing [23] (DIIS), DMFT converges after 60 iterations, whereby we consider the calculation to be converged if for both the self-energy and the impurity Green's function the difference between successive iterations averaged over the first ten Matsubara frequencies does not exceed a relative tolerance of one percent for ten consecutive iterations.

First, we study the average occupation numbers of the Ce- $4f_{5/2}$ orbitals as a function of temperature. For a converged DMFT calculation they can be directly obtained from the average occupations of the impurity. In total we have 1.02 $4f$ electrons in DMFT, i.e., a Ce³⁺ configuration. This is not so different in DFT, which yields 0.95 $4f$ electrons. However, there is a substantially larger $J = 7/2$ contribution, as the $J = 7/2$ states are not yet pushed to higher energies by interaction effects; cf. Fig. 2.

Figure 3 shows the partial occupations of the individual $J = 5/2$ states in DMFT. While at room temperature all six orbitals have comparable occupations, the Kondo effect changes this. Specifically, the lower the temperature becomes, the more depleted are the $j_x = \pm 1/2$ and ψ_+ orbitals. The two ψ_- orbitals, however, tend towards being occupied by

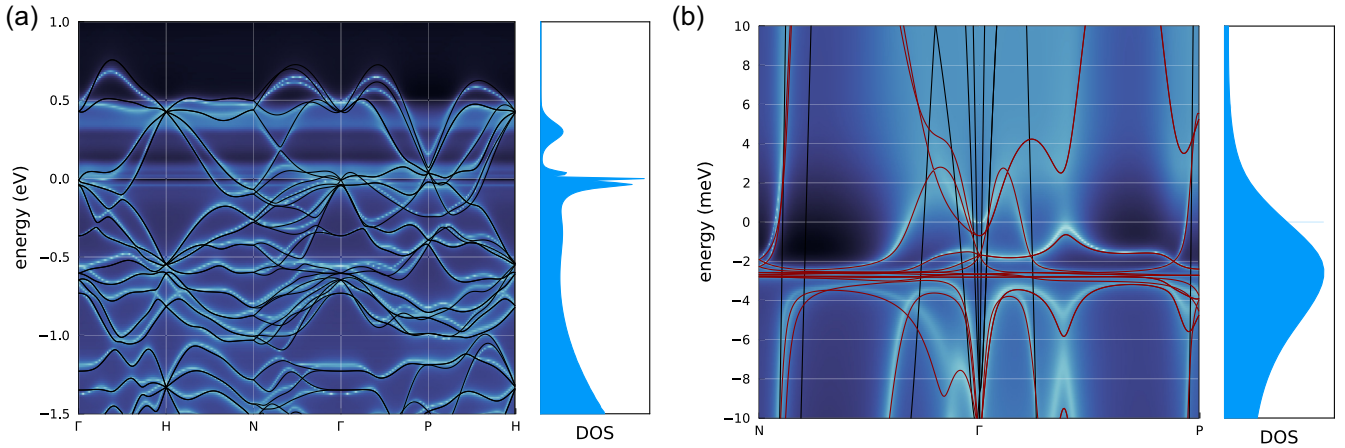


FIG. 4. (a) Momentum-resolved spectral function from DMFT at $T = 29$ K (false color; intensity on logarithmic scale for better visibility). The black curve is the DFT band structure where the Ce-4*f* orbitals are treated in the open-core approximation. The rightmost panel of (a) shows the partial density of states of the ψ_- Ce-4*f*_{5/2} orbital with an emerging Kondo resonance. (b) Zoom-in along N- Γ -P. Close to the Fermi energy the quasiparticle Hamiltonian from Eq. (5) (red curve) agrees much better with DMFT than the open core DFT bands (black).

one electron in total. Hence, at low temperatures solely these 4*f* orbitals with the lowest local crystal field potential are occupied. This state has a local magnetic moment and forms a Kondo resonance through hybridization with the conduction electrons.

In order to resolve this Kondo resonance, we need to analytically continue the imaginary time QMC data obtained within DMFT. This is performed using the maximum entropy method as implemented in Ω MaxEnt [24]. We analytically continue both the local Green's function as well as the self-energy. The imaginary part of the local DMFT Green's function gives us the partial density of states for the Ce-4*f* ψ_- orbital as shown in the right panel of Fig. 4(a). There we can see a Kondo resonance at the Fermi energy $\epsilon_F = 0$ eV. As expected already from the occupations, it has almost solely contributions from the ψ_- orbital.

The k -resolved spectral function in the left panel of Fig. 4(a) is obtained as the imaginary part of the interacting lattice Green's function with the analytically continued DMFT self-energy. Since the DMFT self-consistency loop started from the noninteracting band structure in Fig. 2, which includes hybridization between Ce-4*f* and conduction bands, we can observe how interactions influence the excitation spectrum: At low temperatures a Kondo resonance emerges in the immediate vicinity of the Fermi level.

Seemingly similar dispersions can be observed if we perform a DFT calculation where the Ce-4*f* orbitals are treated in the open-core approximation. The bands from this calculation are shown by the black lines in Fig. 4(a) and are in good agreement with previous results [14].

At high temperatures, open-core DFT is a good approximation to the DMFT spectrum. At lower temperatures, such as $T = 29$ K, in Fig. 4(a) the agreement is still good away from the Fermi energy, i.e., outside the realm of the Kondo resonance. However, in DMFT, flat renormalized quasiparticle bands emerge in the spectral function close to the Fermi energy due to the Kondo effect and show up as essentially horizontal lines in Fig. 4(a). The zoom in Fig. 4(b) shows them more clearly and reveals that they are dispersive on an meV

scale. At $T = 29$ K they are not fully coherent throughout the whole Brillouin zone, as can be seen by a pronounced smearing. However, at temperatures sufficiently smaller than the Kondo temperature this smearing (the imaginary part of the self-energy) is expected to go away. The flat quasiparticle bands will become sharp and, potentially, important for transport. Hence, in the next section we study their topological properties.

If we zoom in on the Fermi edge in Fig. 4(b) we can see that the open core DFT calculation does not capture the renormalized flat bands at all, which shows that they are a consequence of electronic correlations. Energetically the maximum of the Kondo peak is approximately $\omega_0 = 2.4$ meV below the Fermi energy, but with ϵ_F still within the width of the Kondo resonance, as can be seen from the right panel of Fig 4(b). Upon reducing temperature and thus the smearing, the Kondo peak will become sharper, and we expect an upshift of the Kondo resonance since it necessarily forms around ϵ_F .

In the spectral function and in the effective low-energy Hamiltonian discussed in the next section, we do not observe a Kondo insulating gap throughout the full Brillouin zone suggesting semimetallic behavior down to lowest temperatures. We note that the related (isoelectronic) compounds Ce₃Bi₄Pt₃ and Ce₃Sb₄Pt₃ are, instead, prototypical Kondo insulators [25–27]. Owing to their larger Ce-4*f* to conduction state hybridization [28,29], the hybridization gap, while renormalized, remains finite when including correlation effects.

IV. EFFECTIVE LOW-ENERGY HAMILTONIAN

In order to search for Weyl points in the quasiparticle bands, we need an effective single-particle Hamiltonian that captures the low-energy physics of the system. From the DMFT calculation and the analytically continued self-energy $\Sigma(\omega)$ we can determine the momentum-dependent Green's function

$$G(\omega, \mathbf{k}) = (\omega - H_{\mathbf{k}} - \Sigma(\omega) - \Delta_{\text{DC}} + \mu)^{-1}. \quad (3)$$

Here $H_{\mathbf{k}}$ denotes the Bloch-Hamiltonian of the noninteracting Wannier model derived from DFT. The self-energy Σ and the double counting correction Δ_{DC} are diagonal matrices which are nonzero only for the ψ_{-} , ψ_{+} and $j_x = \pm 1/2$ Ce-4 $f_{5/2}$ orbitals. μ is the chemical potential from DMFT.

We expand the Green's function around the maximum of the Kondo resonance ω_0 ,

$$G(\omega, \mathbf{k}) \approx \frac{Z}{\omega - Z^{\frac{1}{2}} [H_{\mathbf{k}} + \Sigma(\omega_0) - \omega_0 \frac{\partial \Sigma(\omega_0)}{\partial \omega} + \Delta_{\text{DC}} - \mu] Z^{\frac{1}{2}}}, \quad (4)$$

where we introduced the quasiparticle renormalization $Z = (1 - \frac{\partial \Sigma(\omega_0)}{\partial \omega})^{-1}$, which can be obtained via numeric differentiation. At the peak maximum ω_0 we find that the imaginary part of the self-energy is minimal and thus Z is real valued.

Equation (4) resembles the Green's function of an effective, renormalized quasiparticle Hamiltonian:

$$H_{\text{qp}}(\mathbf{k}) = Z^{\frac{1}{2}} \left[H_{\mathbf{k}} + \Sigma(\omega_0) - \omega_0 \frac{\partial \Sigma(\omega_0)}{\partial \omega} + \Delta_{\text{DC}} - \mu \right] Z^{\frac{1}{2}}. \quad (5)$$

Taking the square root of Z ensures that Eq. (5) describes a Hermitian operator. We compare its band structure to the DMFT spectral function in Fig. 4(b) (red lines), where we can see that both agree quite well in a region of a few meV around the Fermi energy. The quasiparticle Hamiltonian captures the low-energy excitations due to electronic correlations which the open core DFT calculation (black lines) cannot describe. Therefore, H_{qp} is a good starting point to study whether Ce₃Bi₄Pd₃ exhibits Weyl points in the vicinity of the Fermi energy, which we pursue in the next section.

The reason why the quasiparticle Hamiltonian describes the low-energy excitations better than open core DFT lies in the quasiparticle renormalization Z , which in the present case is small, thereby strongly renormalizing the width of the Ce-4 f bands leading to almost flat bands. This is also an important difference compared to the topological Hamiltonian [30] $H_{\text{topo}}(\mathbf{k}) = G^{-1}(\omega = 0, \mathbf{k})$, which is the inverse of the Green's function evaluated at zero frequency. It differs from H_{qp} by the energy shift $\omega_0 \partial_{\omega} \Sigma(\omega_0)$ and the scaling $Z^{\frac{1}{2}}$. The quasiparticle renormalization is essential to obtain the flat quasiparticle bands close to the Fermi energy which are not present in the topological Hamiltonian.

V. WEYL POINTS IN QUASIPARTICLE BANDS

Now we search for Weyl points in H_{qp} . Since the Wannierization led to a tight-binding Hamiltonian with 192 spin orbitals as described in the previous sections, this search is computationally demanding. Therefore, we employ our recently described algorithm [31] which traces the Berry curvature vector field to its sinks and sources via solving an ordinary differential equation.

We find nine symmetrically inequivalent band crossings in the vicinity of ϵ_F , each of which sits at general momenta away from high-symmetry lines. We confirm that these are Weyl points by calculating the corresponding Chern numbers numerically. Due to time reversal and the 24 point group symmetries, each Weyl node is 48-fold degenerate, i.e., it belongs to a set of 48 nodes related by symmetry. As half of the point

TABLE I. Weyl points of the quasiparticle Hamiltonian. Their locations are listed in Cartesian coordinates rounded to three digits. We present only those Weyl points that belong to bands closest to the Fermi energy, but others exist too. Due to symmetry, each point is 48-fold degenerate. In Fig. 8 in Appendix B we show these degenerate locations for the first Weyl point from this table. The dispersion around the second Weyl point (indicated in boldface) is shown in Fig. 5.

Location ($2\pi/a$)	Energy (meV)	Type
(0.584, 0.082, -0.225)	-1.26	II
(-0.568, -0.394, -0.691)	-1.75	II
(0.559, 0, -0.289)	-2.14	I
(-0.354, 0, -0.496)	-2.42	II
(-0.371, -0.728, -0.495)	7.27	II
(-0.348, 0.398, 0.181)	21.08	II
(0.262, 0, -0.493)	26.18	II
(-0.251, -0.559, -0.006)	26.35	II
(0.574, 0, 0.228)	26.41	II

group symmetries have negative determinants, each of these sets can be split into two halves of nodes having opposite Chern numbers. Hence, the Nielsen-Ninomiya theorem which enforces a total of zero Chern numbers [32,33] is fulfilled.

Four sets of Weyl points are a few meV below, and five a few meV above the Fermi edge. From the eigenstates of H_{qp} we can infer that the former four sets belong to bands whose character is around 90% to 99% of the ψ_{-} 4 $f_{5/2}$ orbital. The latter five sets above ϵ_F have predominantly $j_x = \pm 1/2$ character. We list them in Table I and exemplarily show the second Weyl point in Fig. 5. By comparing the band structure of the effective quasiparticle Hamiltonian H_{qp} (red lines) to the momentum-resolved spectral function from DMFT (color

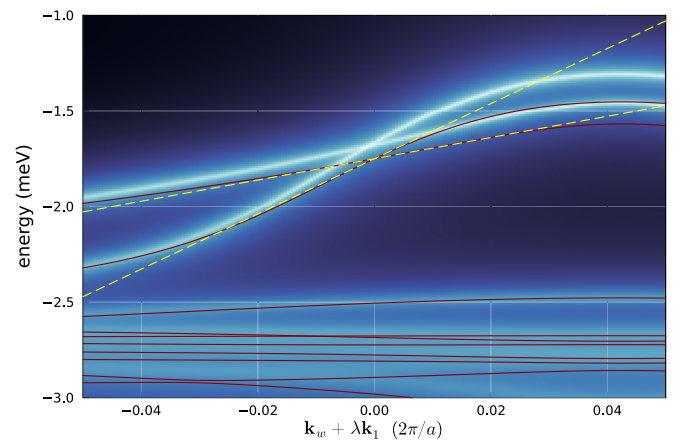


FIG. 5. At $T = 29\text{K}$ the quasiparticle renormalized Hamiltonian H_{qp} from Eq. (5) has a Weyl point a few meV below the Fermi energy (red lines). These band crossings can also be found in the momentum resolved spectral function with the DMFT self-energy (logarithmic color scale). Since the tangents of both crossing bands (yellow dashed lines) have positive slope, we can infer that this is a type II Weyl point. The path in momentum space is chosen as $\mathbf{k}_W + \lambda \mathbf{k}_1$ where \mathbf{k}_W is the momentum of the second Weyl point from Table I, \mathbf{k}_1 is the first primitive basis vector, and $\lambda \in [-0.05, 0.05]$.

scale), we can see that this band crossing is present in both of them.

With energies differing only on a sub-meV scale compared to the DMFT spectral function, H_{qp} is a sufficiently good approximation to detect Weyl points in momentum space. The reason for small energetic offsets is that H_{qp} is obtained from an expansion of the DMFT Green's function around the maximum of the Kondo peak. If we go away from this peak, we must expect some deviations in energy. However, as long as these deviations do not become large enough to drastically move the Weyl points or create or annihilate them in pairs, H_{qp} can be used to search for topological band crossings and compare them to the DMFT spectral function. At least this is the case for the four Weyl nodes below the Fermi edge; those five above are too far away in energy from the maximum of the expansion for a meaningful comparison of the results from H_{qp} to the DMFT spectral function. Furthermore, as discussed earlier, they have predominantly $j_x = \pm 1/2$ character. Hence, to study these it would be better to obtain H_{qp} from an expansion around the peak energies of these orbitals.

The plot reveals the type II nature of the Weyl node, which can be inferred from the slopes of the crossing bands having the same sign [8,34,35]. This discovery of a type II Weyl point supports the interpretation of the spontaneous Hall effect seen in experiment. Furthermore, its type II nature impacts the temperature dependence of specific heat capacity c_V . While a type I Weyl node has a pointlike Fermi surface and therefore leads to a cubic temperature dependence of c_V [1,6], a type II node is embedded in a finite Fermi surface [34] such that the specific heat has terms linear and cubic in temperature. This reasoning can be confirmed by calculating c_V for variable temperatures T from the quasiparticle Hamiltonian via

$$c_V = \frac{1}{(2\pi)^3} \sum_n \int \epsilon_n(\mathbf{k}) \frac{\partial f(\epsilon_n(\mathbf{k}))}{\partial T} d^3k \quad (6)$$

with the chemical potential fixed to the energy of the first Weyl point in Table I. Here $\epsilon_n(\mathbf{k})$ are the eigenvalues of H_{qp} and f is the Fermi-Dirac distribution. The integral over momenta is performed numerically. We fit $c_V = aT + bT^3$ to these data. From the cubic term we can calculate the quasiparticle velocity [1,6] via $v^* = \sqrt[3]{7\pi^2 k_B / (30b)}$ yielding approximately 245 m/s. Similar to the experimental results [1] this is three orders of magnitude smaller than for usual, weakly interacting metals because of the flatness of the quasiparticle bands. Hence, our calculations support the experimental findings qualitatively. Quantitatively, however, our result is by a factor of 3.6 smaller than experiment, likely due to the fact that here we used the quasiparticle Hamiltonian to determine c_V . This includes additional contributions to c_V besides those from the Weyl nodes, which results in a nonvanishing linear in temperature term (aT). It does not account for temperature-dependent changes of the correlated band structure, and we also do not know the precise position of the chemical potential at the experimental temperature. For a quantitatively accurate specific heat, further contributions from the interaction energy and band effects beyond the quasiparticle linearization are likely important. This would, however, require DMFT calculations for temperatures between 2 and 10 K, which is not feasible at present.

TABLE II. Weyl points from DFT where Ce-4*f* orbitals are treated in the open-core approximation. Their locations are listed in Cartesian coordinates rounded to three digits.

Location ($2\pi/a$)	Energy (meV)	Type
(−0.77, −0.862, −0.656)	−18.1	II
(−0.418, −0.566, −0.348)	−43.0	II
(0.527, −0.142, 0.274)	−118	II
(0.546, 0, −0.231)	−132	II
(0.07, −0.438, −0.324)	−157	II
(−0.395, 0, 0.425)	−161	II
(0.182, 0, 0.464)	−180.7	II
(−0.145, −0.426, 0.253)	−181.4	II
(−0.587, −0.769, −0.802)	−196	II
(0.109, 0, 0.39)	−208	I
(0.494, 0.0, −0.248)	247	II
(0.705, 0, −0.129)	−310	II
(0.114, 0.571, −0.223)	318	I
(−0.779, −0.782, −0.992)	−420	II

To test the stability of our findings we apply the procedure described above to the quasiparticle Hamiltonian (5) obtained from the self energy of the converged DMFT calculation and from the self-energy averaged over the last five DMFT iterations. It turns out that although the height of the Kondo resonance fluctuates slightly, the momenta of the Weyl points are almost unaffected. This reflects the fact that Weyl points are topological properties of the band structure and hence small perturbations of the system do not remove them unless the perturbation is large enough to annihilate them in pairs, which is not the case here.

On the other hand, the topological character of the Weyl nodes raises the question whether these nodes are already present at the DFT level, but adiabatically moved to different positions in energy and momentum. In the case of the DFT calculation including the Ce-4*f* orbitals, there is a band gap (which closes within DMFT). Hence, the DFT Hamiltonian and the quasiparticle Hamiltonian H_{qp} are not adiabatically connected. Consequently, we cannot expect that they share topological features, and indeed we did not find Weyl points close to the Fermi edge in the DFT Hamiltonian. Thus, the low-energy Weyl points are correlation-induced.

Due to the apparent similarity of the DFT bandstructure where Ce-4*f* orbitals are treated in the open-core approximation and the DMFT spectral function in Fig. 4(a), we revisit the former and perform a search for Weyl points with the same algorithm [31] as above. We detect multiple Weyl points as listed in Table II, which also includes Weyl points that had not been found in an earlier study [5]. Some of these also appear in the DMFT spectral function at almost the same momentum and energy. Others may change their position or be pairwise annihilated. However, none of them are as close to the Fermi edge as the Weyl nodes from the renormalized quasiparticle bands.

Beyond this disparity, there is an important physical distinction between the two settings. The open-core DFT calculation, used previously to advocate a topological state in Ce₃Bi₄Pd₃ [14], mimics effectively localized *f* states, corresponding to the *high-temperature* local-moment regime. The

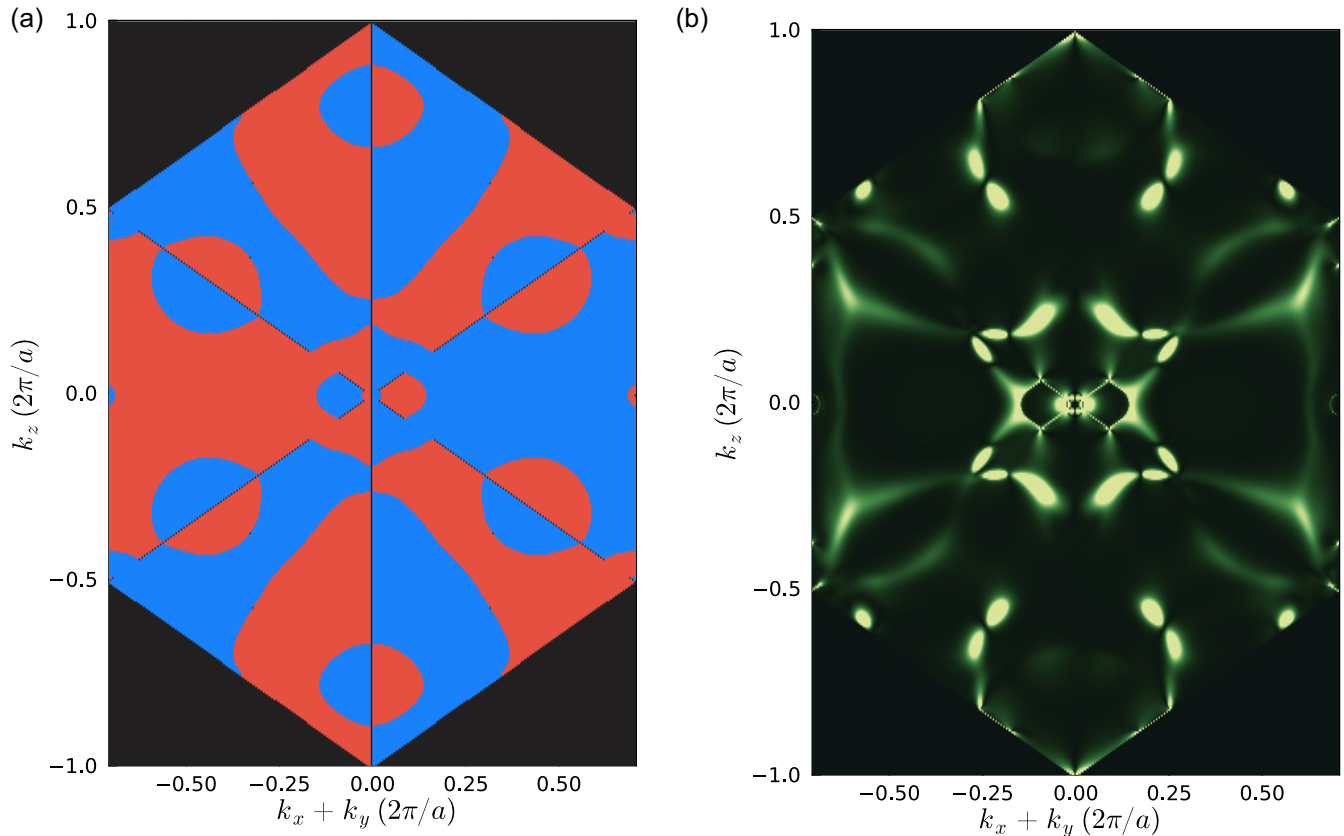


FIG. 6. (a) Eigenvalues of glide mirror symmetry in the plane spanned by k_z and $k_x + k_y$ for a renormalized quasiparticle band: red and blue denote $\pm i$, respectively. The boundaries of areas of different mirror eigenvalues are nodal lines. (b) Magnitude (norm) of Berry curvature in the same plane. By comparison with (a) we see that Berry curvature is large near some of the nodal lines, but also at other points.

signatures of the topological state, however, are observed at very *low temperatures*, where an additional Kondo resonance emerges due to many-body effects. This yields the flat renormalized quasiparticle bands close to the Fermi edge which are not present in DFT and are essential for the existence of the discussed Weyl nodes. The apparent similarity of the conduction band dispersions thus does not justify a meaningful analysis of topology on the basis of DFT.

VI. NODAL LINES IN QUASIPARTICLE BANDS

Besides Weyl nodes other types of topological band crossings are possible. One example is the nodal line where bands are degenerate on a curve in momentum space. A previous study [14] found nodal lines in their Bloch Hamiltonian from a DFT calculation with Ce-4*f* orbitals treated in the open-core approximation as well as in the *topological* Hamiltonian [30] extracted from their DMFT calculation. Here we study whether the renormalized bands from the *quasiparticle* Hamiltonian also have nodal lines within a few meV around the Fermi energy.

In crystals that exhibit a glide mirror plane, as is the case in $\text{Ce}_3\text{Bi}_4\text{Pd}_3$, each band has a well-defined mirror eigenvalue within the corresponding plane in reciprocal space. Bands with different eigenvalues do not interact with each other, and hence they may cross on a line in this plane instead of at an isolated point [36].

$\text{Ce}_3\text{Bi}_4\text{Pd}_3$ has six glide mirror planes in which we can search for nodal lines. As we are considering a spinful system, the glide mirror eigenvalues of the bands at momentum \mathbf{k} are $\lambda = \pm i e^{i\mathbf{k}\cdot\boldsymbol{\tau}}$ where $\boldsymbol{\tau}$ is the translation vector of the glide mirror symmetry operation [37]. These eigenvalues are smooth functions of momentum unless two bands cross. Thus by searching such discontinuities, we can identify nodal lines. To put it differently, $\lambda e^{-i\mathbf{k}\cdot\boldsymbol{\tau}}$ is constant on patches of the mirror plane that are bounded by nodal lines.

Since all glide mirror planes are conjugate to each other, i.e., symmetrically equivalent, we exemplarily show these patches of constant mirror eigenvalue in the plane perpendicular to $(1, -1, 0)$ centered at $\mathbf{k} = 0$ in Fig. 6(a) for a quasiparticle band close to the Fermi energy. We obtain multiple nodal lines as can be seen by the many patches. The nodal lines near the center cross the Fermi energy and thus may contribute to the specific heat and spontaneous Hall effect. The ellipsoidal ones at the top and bottom are about 20 meV above; the remaining four ellipsoidal nodal lines are about 2 meV below.

To demonstrate the effect of the nodal lines on the Berry curvature, we plot the norm (or magnitude) of the latter for the same mirror plane in Fig. 6(b). By comparison with Fig. 6(a) we see that not all nodal lines cause a large contribution to the curvature, and most of it is concentrated in the central Brillouin zone region. Conversely, there are also Berry curvature contributions of similar magnitude which do not follow the

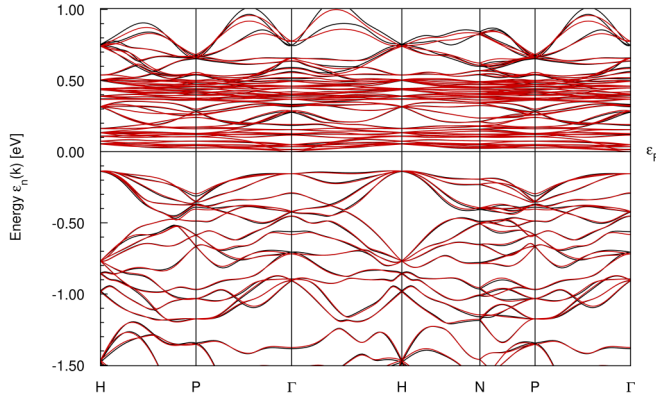


FIG. 7. Comparison between the Kohn-Sham bands from DFT (black) and the bands of the Wannier Hamiltonian from Wannierization (red).

nodal lines. They show up as bright spots in the plot but do not belong to singularities in the mirror plane [38].

VII. CONCLUSION

We studied the Kondo semimetal $\text{Ce}_3\text{Bi}_4\text{Pd}_3$ within DFT and DMFT and observed that a Kondo resonance emerges involving only two out of the six $\text{Ce-}4f_{5/2}$ orbitals (the ψ_- combination of $j_x = \pm 3/2$ and $\mp 5/2$). Below the Kondo temperature, these are the only occupied $4f$ orbitals, whereas at elevated temperatures all six $\text{Ce-}4f_{5/2}$ orbitals are filled more equally. This theoretical prediction can be tested in future resonant inelastic x-ray (RIXS) and x-ray absorption experiments [39].

The dispersion of the two ψ_- $\text{Ce-}4f_{5/2}$ orbitals in DMFT is qualitatively different from DFT and from DFT with the $4f$'s in the open core. It shows Weyl nodes close to the Fermi surface. This strengthens the interpretation of $\text{Ce}_3\text{Bi}_4\text{Pd}_3$ being a Weyl-Kondo semimetal from transport measurements [1,5].

Furthermore, multiple nodal lines in mirror planes provide Berry curvature near the Fermi energy that could, similarly to the Weyl points, contribute to the giant spontaneous Hall effect [5]. Weyl points and nodal lines are within only 3 meV of the Fermi energy at the lowest temperature reached in our calculation. There the Kondo peak is not yet fully developed. Hence, it appears likely that the Weyl points hit the Fermi energy when the Kondo peak further sharpens and shifts upon lowering temperature or when marginally doping $\text{Ce}_3\text{Bi}_4\text{Pd}_3$.

The DFT and DMFT data are available from [40].

ACKNOWLEDGMENTS

We thank Silke Paschen, Anna Kauch, and Markus Wallerberger for very helpful discussions. This work has been supported by the Austrian Science Fund (FWF) through SFB Q-M&S (FWF project ID F86) and the Research Unit

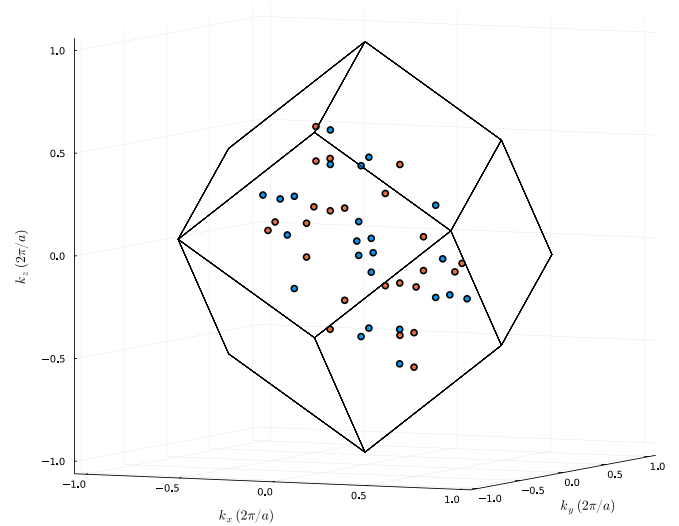


FIG. 8. Symmetrically equivalent positions in the Brillouin zone of the first Weyl point from Table I. The different colors reflect opposite Chern numbers.

FOR5249 ‘QUAST’ by the Deutsche Forschungsgemeinschaft with funding obtained through FWF project ID I 5868. Calculations have been mainly done on the Vienna Scientific Cluster (VSC).

APPENDIX A: WANNIERIZATION

To judge the quality of our Wannierization of the Kohn-Sham bands from DFT we compare the latter to the bands of the Wannier Hamiltonian in Fig. 7. We observe good agreement near the band gap. Farther away from it small deviations appear. However, we expect that these will not significantly affect the low-energy physics, especially neither the Kondo resonance nor the quasiparticle bands observed in DMFT.

For calculation of the densities of states in Fig. 2 we used the Wannier Hamiltonian to interpolate the bands on a dense, equally spaced $50 \times 50 \times 50$ grid in order to numerically perform the momentum integration. A Gaussian broadening with standard deviation $\sigma = 10$ meV has been used.

APPENDIX B: WEYL POINTS IN QUASIPARTICLE BANDS

To give a better overview on how the Weyl points found within DMFT are located in the Brillouin zone we exemplarily show the symmetrically equivalent positions of the Weyl node closest to the Fermi energy in Fig. 8. Note that a projection of a 3D plot distorts the image such that the symmetry operations relating the different points might not be recognizable. Hence, we computationally confirmed that these positions are actually related by the point group symmetry of the crystal. For a closer hands-on inspection of the Weyl points we further provide as Supplemental Material a rotatable version of Fig. 8 [41].

[1] S. Dzsaber, L. Prochaska, A. Sidorenko, G. Eguchi, R. Svagera, M. Waas, A. Prokofiev, Q. Si, and S. Paschen, Kondo insulator to semimetal transformation tuned by spin-orbit coupling, *Phys. Rev. Lett.* **118**, 246601 (2017).

[2] Y. Xu, C. Yue, H. Weng, and X. Dai, Heavy Weyl fermion state in CeRu_4Sn_6 , *Phys. Rev. X* **7**, 011027 (2017).

[3] C. Guo, C. Cao, M. Smidman, F. Wu, Y. Zhang, F. Steglich, F.-C. Zhang, and H. Yuan, Possible Weyl fermions in the

- magnetic Kondo system CeSb, *npj Quantum Mater.* **2**, 39 (2017).
- [4] C. Y. Guo, F. Wu, Z. Z. Wu, M. Smidman, C. Cao, A. Bostwick, C. Jozwiak, E. Rotenberg, Y. Liu, F. Steglich *et al.*, Evidence for Weyl fermions in a canonical heavy-fermion semimetal YbPtBi , *Nat. Commun.* **9**, 4622 (2018).
- [5] S. Dzsaber, X. Yan, M. Taupin, G. Eguchi, A. Prokofiev, T. Shiroka, P. Blaha, O. Rubel, S. E. Grefe, H.-H. Lai *et al.*, Giant spontaneous Hall effect in a nonmagnetic Weyl–Kondo semimetal, *Proc. Natl. Acad. Sci. USA* **118**, e2013386118 (2021).
- [6] H.-H. Lai, S. E. Grefe, S. Paschen, and Q. Si, Weyl–Kondo semimetal in heavy-fermion systems, *Proc. Natl. Acad. Sci. USA* **115**, 93 (2018).
- [7] C. Herring, Accidental degeneracy in the energy bands of crystals, *Phys. Rev.* **52**, 365 (1937).
- [8] N. P. Armitage, E. J. Mele, and A. Vishwanath, Weyl and Dirac semimetals in three-dimensional solids, *Rev. Mod. Phys.* **90**, 015001 (2018).
- [9] G. E. Volovik, Zeros in the fermion spectrum in superfluid systems as diabolical points, *Pis'ma Zh. Eksp. Teor. Fiz.* **46**, 81 (1987) [*JETP Lett.* **46**, 81 (1987)].
- [10] F. D. M. Haldane, Berry curvature on the Fermi surface: Anomalous Hall effect as a topological Fermi-liquid property, *Phys. Rev. Lett.* **93**, 206602 (2004).
- [11] W. Hermes, S. Linsinger, R. Mishra, and R. Pöttgen, Structure and properties of $\text{Ce}_3\text{Pd}_3\text{Bi}_4$, CePdBi , and CePd_2Zn_3 , *Monatsh. Chem.-Chem. Mon.* **139**, 1143 (2008).
- [12] G. Kotliar, S. Y. Savrasov, K. Haule, V. S. Oudovenko, O. Parcollet, and C. A. Marianetti, Electronic structure calculations with dynamical mean-field theory, *Rev. Mod. Phys.* **78**, 865 (2006).
- [13] K. Held, Electronic structure calculations using dynamical mean field theory, *Adv. Phys.* **56**, 829 (2007).
- [14] C. Cao, G.-X. Zhi, and J.-X. Zhu, From trivial Kondo insulator $\text{Ce}_3\text{Pt}_3\text{Bi}_4$ to topological nodal-line semimetal $\text{Ce}_3\text{Pd}_3\text{Bi}_4$, *Phys. Rev. Lett.* **124**, 166403 (2020).
- [15] K. Koepnick and H. Eschrig, Full-potential nonorthogonal local-orbital minimum-basis band-structure scheme, *Phys. Rev. B* **59**, 1743 (1999).
- [16] J. P. Perdew and Y. Wang, Accurate and simple analytic representation of the electron-gas correlation energy, *Phys. Rev. B* **45**, 13244 (1992).
- [17] A. P. Cracknell, B. L. Davies, and S. C. Miller, *General Introduction and Tables of Irreducible Representations of Space Groups*, Kronecker product tables (IFI/Plenum, 1979).
- [18] M. Wallerberger, A. Hausoel, P. Gunacker, A. Kowalski, N. Parragh, F. Goth, K. Held, and G. Sangiovanni, w2dynamics: Local one- and two-particle quantities from dynamical mean field theory, *Comput. Phys. Commun.* **235**, 388 (2019).
- [19] J. M. Tomczak, Realistic many-body theory of Kondo insulators: Renormalizations and fluctuations in $\text{Ce}_3\text{Bi}_4\text{Pt}_3$, [arXiv:1904.01346](https://arxiv.org/abs/1904.01346) (2019).
- [20] C. Xu, C. Cao, and J.-X. Zhu, Pressure-induced concomitant topological and metal-insulator quantum phase transitions in $\text{Ce}_3\text{Pd}_3\text{Bi}_4$, *npj Quantum Mater.* **7**, 18 (2022).
- [21] M. O. Ajeesh, S. K. Kushwaha, S. M. Thomas, J. D. Thompson, M. K. Chan, N. Harrison, J. M. Tomczak, and P. F. S. Rosa, Localized f -electron magnetism in the semimetal $\text{Ce}_3\text{Bi}_4\text{Au}_3$, *Phys. Rev. B* **108**, 245125 (2023).
- [22] V. I. Anisimov, A. I. Poteryaev, M. A. Korotin, A. O. Anokhin, and G. Kotliar, First-principles calculations of the electronic structure and spectra of strongly correlated systems: Dynamical mean-field theory, *J. Phys.: Condens. Matter* **9**, 7359 (1997).
- [23] P. Pulay, Convergence acceleration of iterative sequences. The case of SCF iteration, *Chem. Phys. Lett.* **73**, 393 (1980).
- [24] D. Bergeron and A.-M. S. Tremblay, Algorithms for optimized maximum entropy and diagnostic tools for analytic continuation, *Phys. Rev. E* **94**, 023303 (2016).
- [25] M. F. Hundley, P. C. Canfield, J. D. Thompson, Z. Fisk, and J. M. Lawrence, Hybridization gap in $\text{Ce}_3\text{Bi}_4\text{Pt}_3$, *Phys. Rev. B* **42**, 6842 (1990).
- [26] C. D. W. Jones, K. A. Regan, and F. J. DiSalvo, Thermoelectric properties of the doped Kondo insulator: $\text{Nd}_x\text{Ce}_{3-x}\text{Pt}_3\text{Sb}_4$, *Phys. Rev. B* **58**, 16057 (1998).
- [27] J. M. Tomczak, Thermoelectricity in correlated narrow-gap semiconductors, *J. Phys.: Condens. Matter* **30**, 183001 (2018).
- [28] J. M. Tomczak, Isoelectronic tuning of heavy fermion systems: Proposal to synthesize $\text{Ce}_3\text{Sb}_4\text{Pd}_3$, *Phys. Rev. B* **101**, 035116 (2020).
- [29] M. O. Ajeesh, S. M. Thomas, S. K. Kushwaha, E. D. Bauer, F. Ronning, J. D. Thompson, N. Harrison, and P. F. S. Rosa, Ground state of $\text{Ce}_3\text{Bi}_4\text{Pd}_3$ unraveled by hydrostatic pressure, *Phys. Rev. B* **106**, L161105 (2022).
- [30] Z. Wang and B. Yan, Topological Hamiltonian as an exact tool for topological invariants, *J. Phys.: Condens. Matter* **25**, 155601 (2013).
- [31] M. Braß, L. Si, and K. Held, Weyl points and spin-orbit coupling in copper-substituted lead phosphate apatite, *Phys. Rev. B* **109**, 085103 (2024).
- [32] H. B. Nielsen and M. Ninomiya, Absence of neutrinos on a lattice: (I). Proof by homotopy theory, *Nucl. Phys. B* **185**, 20 (1981).
- [33] H. B. Nielsen and M. Ninomiya, Absence of neutrinos on a lattice: (II). Intuitive topological proof, *Nucl. Phys. B* **193**, 173 (1981).
- [34] A. A. Soluyanov, D. Gresch, Z. Wang, Q. Wu, M. Troyer, X. Dai, and B. A. Bernevig, Type-II Weyl semimetals, *Nature (London)* **527**, 495 (2015).
- [35] Y. Xu, F. Zhang, and C. Zhang, Structured Weyl points in spin-orbit coupled fermionic superfluids, *Phys. Rev. Lett.* **115**, 265304 (2015).
- [36] C. Fang, H. Weng, X. Dai, and Z. Fang, Topological nodal line semimetals, *Chin. Phys. B* **25**, 117106 (2016).
- [37] S. M. Young and C. L. Kane, Dirac semimetals in two dimensions, *Phys. Rev. Lett.* **115**, 126803 (2015).
- [38] In principle they could correspond to Weyl nodes outside the plane, but the ones we found in the previous section are far away from these spots.
- [39] For an experiment resolving the crystal field splitting of a $4f$ systems, see, e.g., [42].
- [40] <https://doi.org/10.48436/3zxm-q6f44>
- [41] The Supplemental Material at <http://link.aps.org/supplemental/10.1103/PhysRevResearch.6.033227> shows a rotatable version of Fig. 8.
- [42] M. Sundermann, F. Strigari, T. Willers, H. Winkler, A. Prokofiev, J. M. Ablett, J.-P. Rueff, D. Schmitz, E. Weschke, M. M. Sala *et al.*, CeRu_4Sn_6 : A strongly correlated material with nontrivial topology, *Sci. Rep.* **5**, 17937 (2015).